J. Fluid Mech. (2002), *vol.* 473, *pp.* 389–411.
DOI: 10.1017/S0022112002002562 Printed in the United Kingdom

The stability of a slowly diverging swirling jet

By A. J. COOPER† AND N. PEAKE

Department of Applied Mathematics and Theoretical Physics, University of Cambridge, Silver Street, Cambridge CB3 9EW, UK

(Received 15 October 2001 and in revised form 13 May 2002)

The spatial evolution of small-amplitude unsteady disturbances of an axisymmetric swirling jet is examined theoretically. The slow axial divergence of the jet mean flow is accounted for by using the method of multiple scales and a consistent solution for both the mean flow and unsteady disturbance is derived. Previous work by Lu & Lele (1999) has considered the leading-order analysis, in which the modal eigenvalues are determined from locally parallel theory, but the key feature of our analysis is the solution of the next-order secularity condition for the axial variation of the wave-envelope amplitude.

The swirling jet profile sustains two types of instability waves: the Kelvin–Helmholtz instability associated with axial shear, and a centrifugal instability which arises due to a decrease in circulation with radial distance. The evolution of the disturbance axial wavenumber and envelope amplitude with downstream distance is calculated. Numerical results show that the growth of the centrifugal mode is significantly curtailed as a result of a rapidly decaying envelope amplitude. The shear instability is significantly more amplified by the addition of swirl.

The general solution for the disturbance envelope amplitude breaks down at so-called turning points. This is found to occur for a series of neutral propagating modes. A rescaling in the vicinity of the turning point shows that the amplitude in this region is governed by a parabolic cylinder equation. The modal amplitude is seen to decay very significantly through this turning point, even though the mode is neutral to leading order.

1. Introduction

Many natural and industrial fluid flows have strong vorticity. One type of vortical flow which is of practical interest is the swirling jet, which has been shown to be more unstable than its non-swirling counterpart. A particular application, where such increased instability is desirable, is to add swirl to axisymmetric jets as a means of mixing enhancement. This is particularly relevant to the renewed industrial interest in scramjet engines (supersonic combustion ram jets) where the mixing of fuel and oxidizer must occur over a short time. Since non-swirling jet flow tends to become more stable with increased compressibility, the addition of swirl to these systems may lead to more efficient combustion. Jet noise and jet-plume growth are further areas motivating the study of compressible mixing layers.

A number of theoretical investigations into the effects of swirl on the instability of axisymmetric jet flow have been undertaken. Khorrami (1995) showed, using temporal linear stability analysis, how the presence of swirl could enhance instability growth

† Present address: School of Engineering, University of Warwick, Coventry CV4 7AL, UK.

rates and also give rise to regions of instability which are absent in a non-swirling flow. The stabilizing effect of increasing Mach number was also found to be less pronounced with the addition of swirl. As well as enhancing the axial shear, or Kelvin–Helmholtz, instability the swirling jet can also support centrifugal instability which arises due to a decrease in the circulation with radial distance.

Some investigators have used a basic analytical model of a swirling jet to study instability characteristics. Martin & Meiburg (1994) studied a top-hat jet, with swirl added in the form of free vortex flow inside the jet core and a second free vortex in the external flow. They found that the type of instability favoured depends on the difference between the inner and outer circulations. The absolute and convective nature of instability in a similar family of swirling jets/wakes was investigated by Loiseleux, Delbende & Huerre (2000). Centrifugally stabilizing or destabilizing swirl differences were found to promote absolute instability. Lim & Redekopp (1998) also studied absolute instability characteristics and included the effects of density variation. One of the flows considered was an axial flow with solid-body rotation within the jet core and a free vortex flow outside the core. The swirl velocity was permitted to be discontinuous at the edge of the jet. Increases in the size of this discontinuity were found to increase the absolute growth rate considerably. Changes in relative density between the core and external flow were also found to affect the growth rate.

The influence of viscosity has been investigated by Sarasúa & Schifino (2000). Their jet profile consisted of a top-hat axial flow with a non-rotating core and free vortex flow outside the core. A numerical study revealed that viscous effects can induce instability in regions that are stable in inviscid flows.

Experimental work by Naughton, Cattafesta & Settles (1997) on jets with variable degrees of swirl and compressibility suggested that increases in entrainment of up to 60% could be achieved with the addition of swirl. Wu, Farokhi & Taghavi (1992) also carried out some experimental work on a top-hat jet with solid-body rotation inside the jet and free vortex flow outside the core, together with some theoretical work aimed at developing an understanding of shear-layer control with swirl. Cutler, Levey & Kraus (1995) describe an efficient method of generating swirling jets by tangential injection, and also found increased mixing compared to non-swirling jets.

More recently Hu, Sun & Yin (2001) have carried out a direct numerical simulation to study the dynamics of a temporally evolving swirling jet. Results suggested several possible mechanisms for the enhancement of mixing by swirl, such as the radial motion of vortex ring pairs, the rapid growth of streamwise vorticity and the creation of three-dimensional small eddies.

Lu & Lele (1999) considered a slightly different form of swirling jet profile to those described above, with the swirl velocity being confined to the region of the shear layer, as might be the case if the swirl is induced by the introduction of tabs on the jet nozzle. Another difference to previous theoretical work is that the axial evolution of the jet mean flow was calculated using the boundary layer equations. Spatial instability analysis was mainly restricted to the flow at a fixed axial location, but the effect of the mean flow development on the instability characteristics was briefly discussed. Again it was found that swirl significantly increases the maximum amplification rate in incompressible flow, and that this effect is repeated when compressibility effects are included. The disturbance energy was also analysed, and this showed that the shear in the swirl component contributes to a significant proportion of the disturbance energy.

With the exception of Lu & Lele's paper, existing theoretical work on swirling jets has been restricted to parallel flows and simplified velocity profiles. In this paper, we follow Lu & Lele, in that the axial development of the mean flow is included, and an

explicit, consistent multiple-scales solution is derived for both the mean flow and the disturbance. This then allows the prediction of both disturbance growth rates (as done by Lu & Lele) and, importantly, envelope amplitudes as functions of axial distance. The determination of the axial variation of the disturbance envelope amplitude is not attempted in Lu & Lele, and is the principal contribution of the present paper. The total amplitude of a mode depends on both the envelope amplitude and (for non-neutral modes) on the integrated growth rate, and we will see subsequently that the spatial evolution of the envelope amplitude can have a significant effect on the behaviour of the mode. This type of analysis has been studied previously for non-swirling jets and mixing layers by Bouthier (1972, 1973), Crighton & Gaster (1976), Tam & Burton (1984*a*, *b*) and Tam & Morris (1980). The work by Tam and co-investigators also considers sound generation by instability waves in non-parallel axisymmetric jets and mixing layers.

The divergence of jet flows is an important factor to consider, because the resulting instability characteristics show a significant departure from those predicted by the parallel flow approximation. Close to the nozzle exit, where the shear layer is thin, unstable waves grow rapidly. However, as they propagate downstream the mean flow diverges, the growth rate is reduced and at some location downstream the waves eventually become damped. Therefore the indefinite growth predicted by the parallel flow approximation applied near the nozzle is curtailed. The envelope amplitude of the disturbance also decays as the wave propagates downstream, and Tam & Burton (1984*a*, *b*) demonstrate how this growth and decay of disturbance amplitude is a significant factor in the radiation of sound. It is important to know whether the enhanced growth rate in jet flows due to the addition of swirl is sustained when the axial development of the base flow is accounted for. Non-parallel effects are included by applying the WKB technique whereby a small parameter, $\varepsilon \ll 1$, is introduced which characterizes the slow divergence of the jet. In fact, ε is the inverse of a typical Reynolds number, so that viscous terms become confined to $O(\varepsilon)$, and these effects then contribute to the axial variation of the disturbance amplitude.

The general problem formulation is described in § 2, with the multiple-scales solution for the mean flow in § 3. The method for obtaining the disturbance growth rate and amplitude follows in § 4. Numerical results for a particular set of flow conditions at the nozzle exit are given in § 5. The general solution for the disturbance amplitude is found to break down under certain conditions and the method for removing the singularity is described in § 6. Conclusions from the investigation are drawn in § 7.

2. Problem formulation

The spatial evolution of small-amplitude unsteady disturbances of an axisymmetric supersonic swirling jet is investigated. At the nozzle exit the axial velocity has a 'near-top-hat' profile with a narrow shear layer. Added to this is an azimuthal, or swirl, velocity; numerical results will be presented for an initial swirl distribution in which the swirl is mainly confined to the shear layer, but the analysis can be applied to a much wider range of nozzle-exit axial and swirl profiles. The jet flow is assumed to be weakly non-parallel so that the axial evolution can be studied using the WKB-type of analysis.

The flow problem is formulated in terms of cylindrical coordinates (x, r, θ), and within the WKB framework the flow field is governed by the compressible boundary-layer equations. Throughout variables are non-dimensionalized using values on the centreline ($r = 0$) at the nozzle exit ($x = 0$). The reference length, velocity, density and

pressure scales are L^*, the vorticity thickness of the axial velocity, U^*, ρ^* and $\rho^* U^{*2}$ respectively. The Reynolds number, based on the inner stream, is defined by

$$Re = \frac{\rho^* U^* L^*}{\mu^*}, \tag{1}$$

where μ^* is the dynamic viscosity. All quantities marked with an asterisk are dimensional.

Since the jet is assumed to be slowly varying it is convenient to introduce a slow axial scale $X = \varepsilon x$, where $\varepsilon \ll 1$ and is a measure of the divergence rate of the jet. Under the assumption of slow divergence viscous effects are also restricted to $O(\varepsilon)$ such that $\varepsilon = 1/Re$.

The total flow field is expressed as the sum of a steady axisymmetric mean flow and an unsteady disturbance field such that

$$[\boldsymbol{v}, \rho, p, \mathscr{T}](X, r, \theta, t) = [\boldsymbol{V}, D, P, T](X, r) + [\tilde{\boldsymbol{v}}, \tilde{\rho}, \tilde{p}, \tilde{\tau}](X, r, \theta, t), \tag{2}$$

where $\boldsymbol{v}$ is the velocity, ρ is the density, p the pressure and $\mathscr{T}$ the temperature.

The governing equations are linearized with respect to the unsteady disturbances, giving rise to a set of linear equations for the disturbance field, and a set of nonlinear equations for the steady mean flow.

3. Mean flow field

The mean flow velocity is given by

$$\boldsymbol{V} = U(X, r; \varepsilon)\boldsymbol{e}_x + V(X, r; \varepsilon)\boldsymbol{e}_r + W(X, r; \varepsilon)\boldsymbol{e}_\theta, \tag{3}$$

and a multiple-scales solution obtained by expanding in powers of ε.

From the steady continuity equation

$$\nabla \cdot (D\boldsymbol{V}) = 0, \quad \text{with} \quad \frac{\partial}{\partial x} = \varepsilon \frac{\partial}{\partial X}, \tag{4}$$

it can be seen that $O(\varepsilon)$ axial variations must be balanced by $O(\varepsilon)$ radial variations. This leads to the following expansions for the mean flow field:

$$U(X, r; \varepsilon) = U_0(X, r) + O(\varepsilon^2), \tag{5}$$
$$V(X, r; \varepsilon) = \varepsilon V_1(X, r) + O(\varepsilon^3), \tag{6}$$
$$W(X, r; \varepsilon) = W_0(X, r) + O(\varepsilon^2), \tag{7}$$
$$D(X, r; \varepsilon) = D_0(X, r) + O(\varepsilon^2), \tag{8}$$
$$P(X, r; \varepsilon) = P_0(X, r) + O(\varepsilon^2), \tag{9}$$
$$T(X, r; \varepsilon) = T_0(X, r) + O(\varepsilon^2). \tag{10}$$

The leading-order mean flow is then governed by the steady continuity, momentum and energy equations, together with the perfect gas assumption. The governing equations and appropriate boundary conditions, given in Lu & Lele (1999), are

$$\frac{\partial (D_0 U_0)}{\partial X} + \frac{1}{r}\frac{\partial (r D_0 V_1)}{\partial r} = 0, \tag{11}$$

$$D_0 U_0 \frac{\partial U_0}{\partial X} + D_0 V_1 \frac{\partial U_0}{\partial r} = -\frac{\partial P_0}{\partial X} + \frac{1}{r}\frac{\partial}{\partial r}\left(\mu_0 r \frac{\partial U_0}{\partial r}\right), \tag{12}$$

$$\frac{D_0 W_0^2}{r} = \frac{\partial P_0}{\partial r}, \tag{13}$$

$$D_0 U_0 \frac{\partial W_0}{\partial X} + \frac{D_0 V_1}{r}\frac{\partial (r W_0)}{\partial r} = \frac{1}{r^2}\frac{\partial}{\partial r}\left(\mu_0 r^3 \frac{\partial}{\partial r}\frac{W_0}{r}\right), \tag{14}$$

$$D_0 U_0 \frac{\partial T_0}{\partial X} + D_0 V_1 \frac{\partial T}{\partial r} = (\gamma - 1)M^2\left(U_0 \frac{\partial P_0}{\partial X} + V_1 \frac{\partial P_0}{\partial r}\right) + \frac{1}{r\sigma}\frac{\partial}{\partial r}\left(\mu_0 r \frac{\partial T_0}{\partial r}\right) \tag{15}$$

$$+ (\gamma - 1)M^2 \mu_0 \left[\left(\frac{\partial U_0}{\partial r}\right)^2 + \left(r\frac{\partial}{\partial r}\frac{W_0}{r}\right)^2\right], \tag{16}$$

$$\gamma M^2 P_0 = D_0 T_0, \tag{17}$$

where γ is the ratio of specific heats. The Prandtl number, σ, and Mach number, M, are defined as

$$\sigma = \frac{\mu^* C_p^*}{k^*}, \quad M = \frac{U^*}{a^*}, \tag{18}$$

where k^* is the thermal conductivity, C_p^* is the specific heat at constant pressure and a^* is the local speed of sound. Following White (1991) and Lu & Lele (1994) the dynamic viscosity is assumed to be a function of temperature only and obeys a power law

$$\mu^* \propto (T^*)^n, \tag{19}$$

where we take $n = 0.67$ for air.

The boundary conditions applied are

$$U_0(X, r \to \infty) = U_2, \ \frac{\partial U_0}{\partial r}(X, r = 0) = 0, \tag{20}$$

$$W_0(X, r \to \infty) = 0, \ V_1(X, r = 0) = 0, \tag{21}$$

$$P_0(X, r \to \infty) = P_2, \ W_0(X, r = 0) = 0, \tag{22}$$

$$T_0(X, r \to \infty) = T_2, \ \frac{\partial T_0}{\partial r}(X, r = 0) = 0, \tag{23}$$

for given values of U_2, P_2 and T_2.

The equations can be solved numerically given a prescribed set of conditions at the nozzle exit. The solution for a particular set of initial conditions is described in § 5.

4. Disturbance field

Using the method of multiple scales the unsteady disturbance field is expressed in terms of a slowly varying amplitude and axial wavenumber in the form

$$[\tilde{\boldsymbol{v}}, \tilde{\rho}, \tilde{p}, \tilde{\tau}](X, r, \theta, t; \varepsilon) = [\hat{\boldsymbol{v}}, \hat{\rho}, \hat{p}, \hat{\tau}](X, r; \varepsilon) \exp\left(\frac{\mathrm{i}}{\varepsilon}\int^X k(\xi)\,\mathrm{d}\xi + \mathrm{i}m\theta - \mathrm{i}\omega t\right), \tag{24}$$

where ω is the frequency, m is the (integer) azimuthal mode number and k is the axial wavenumber. Partial derivatives with respect to x then become

$$\frac{\partial}{\partial x} = \left(\mathrm{i}k(X) + \varepsilon\frac{\partial}{\partial X}\right). \tag{25}$$

If $\hat{\boldsymbol{v}} = [\hat{u}, \hat{v}, \hat{w}]$, then the linearized equations governing the disturbance field, retaining terms up to $O(\varepsilon)$, are

$$E\hat{\rho} + D_0\left(\frac{\hat{v}}{r} + \frac{\partial \hat{v}}{\partial r} + \mathrm{i}k\hat{u} + \frac{\mathrm{i}m\hat{w}}{r}\right) + \hat{v}\frac{\partial D_0}{\partial r} = \varepsilon f_1(\hat{\boldsymbol{v}}, \hat{\rho}, \hat{p}, \hat{\tau}), \tag{26}$$

$$D_0\left(E\hat{u} + \hat{v}\frac{\partial U_0}{\partial r}\right) + \mathrm{i}k\hat{p} = \varepsilon f_2(\hat{\boldsymbol{v}}, \hat{\rho}, \hat{p}, \hat{\tau}), \tag{27}$$

$$D_0\left(E\hat{v} - \frac{2\hat{w}W_0}{r}\right) - \frac{\hat{\rho}W_0^2}{r} + \frac{\partial \hat{p}}{\partial r} = \varepsilon f_3(\hat{\boldsymbol{v}}, \hat{\rho}, \hat{p}, \hat{\tau}), \tag{28}$$

$$D_0\left(E\hat{w} + \frac{\hat{v}W_0}{r} + \hat{v}\frac{\partial W_0}{\partial r}\right) + \frac{\mathrm{i}m\hat{p}}{r} = \varepsilon f_4(\hat{\boldsymbol{v}}, \hat{\rho}, \hat{p}, \hat{\tau}), \tag{29}$$

$$D_0\left(E\hat{\tau} + \hat{v}\frac{\partial T_0}{\partial r}\right) - (\gamma - 1)M^2\left(E\hat{p} + \hat{v}\frac{\partial P_0}{\partial r}\right) = \varepsilon f_5(\hat{\boldsymbol{v}}, \hat{\rho}, \hat{p}, \hat{\tau}), \tag{30}$$

$$\gamma M^2\hat{p} - \hat{\tau}D_0 - \hat{\rho}T_0 = 0, \tag{31}$$

where $E = \mathrm{i}(kU_0 + mW_0/r^2 - \omega)$ and the exact form of the functions $f_1, \ldots, f_5$ are given in the Appendix.

The complex amplitudes are now expanded in powers of ε such that

$$[\hat{\boldsymbol{v}}, \hat{\rho}, \hat{p}, \hat{\tau}](X, r; \varepsilon) = \sum_{n=0}^{\infty} \varepsilon^n [\hat{\boldsymbol{v}}_n, \hat{\rho}_n, \hat{p}_n, \hat{\tau}_n](X, r). \tag{32}$$

Substitution of (32) into (26)–(31) and equating terms of equal order in ε gives, after some rearrangement, a series of equations for the pressure field of the form

$$\mathscr{L}\hat{p}_n = h_n, \tag{33}$$

where $h_0 = 0$ and h_n $(n = 1, 2, \ldots)$ depend on lower-order solutions. The linear operator $\mathscr{L}$ is found in Stott & Duck (1994) and used by Lu & Lele (1999). It is given in the Appendix together with the inhomogeneous terms h_n. It should be noted that the derivation is not strictly valid in the limit of vanishing k.

The boundary conditions for (33) are obtained by considering the form of the equations as $r \to 0, \infty$. In these limits the leading-order equation reduces to a modified Bessel equation as described by Lu & Lele (1999). It then becomes apparent that $h_n \to 0$, and at all orders, (33) is reduced to the form

$$\frac{\partial^2 \hat{p}_n}{\partial r^2} + \frac{1}{r}\frac{\partial \hat{p}_n}{\partial r} - \left(A_j^2 + \frac{m^2}{r^2}\right)\hat{p}_n = 0, \tag{34}$$

where

$$A_j^2 = \left[1 - \frac{D_0^j}{\gamma P_0^j}\left(U_0^j - \frac{\omega}{k}\right)^2\right]k^2, \tag{35}$$

and $j = 1, 2$ denotes values as $r \to 0, \infty$ respectively. In order to have bounded solutions,

$$\hat{p}_n \sim I_m(A_1 r) \quad \text{as} \quad r \to 0, \tag{36}$$

$$\hat{p}_n \sim K_m(A_2 r) \quad \text{as} \quad r \to \infty, \tag{37}$$

where $I_m(A_j r)$ is the modified Bessel function of the first kind, and $K_m(A_j r)$ is the modified Bessel function of the second kind. This asymptotic behaviour is described in Lu & Lele (1999) for the leading-order problem. A solution satisfying both of these conditions can only be found for certain values of k so that (33) is an eigenvalue problem with eigenvalue k.

If p_0 is a solution to the homogeneous problem in (33) then, since $\mathscr{L}$ does not contain any X-derivatives, a general solution is

$$\hat{p}_0(X, r) = N(X) p_0(X, r), \tag{38}$$

where $N(X)$ is an arbitrary function of X. Since all the other leading-order variables ($\hat{u}_0$, $\hat{v}_0$, etc.) are related to $\hat{p}_0$ they also have this same arbitrary factor.

The function $N(X)$ can be determined from the fact that the $n = 1$ equation in (33) is solvable. The solvability condition is obtained by taking the inner product of the $n = 1$ equation with the adjoint solution of the homogeneous problem ($n = 0$). The operator $\mathscr{L}$ is not self-adjoint so that the adjoint operator is to be determined. Since the problem is formulated in terms of cylindrical coordinates the inner product is taken to be

$$\langle \mathscr{A}, \mathscr{B} \rangle = \int_0^\infty \overline{\mathscr{A}} \mathscr{B} r \, \mathrm{d}r, \tag{39}$$

where the overbar denotes the complex conjugate.

With $\mathscr{L}$ as defined in the Appendix, we find that the equation governing the adjoint solution is

$$\mathscr{L}^\dagger p_0^\dagger = 0, \tag{40}$$

where

$$\mathscr{L}^\dagger \equiv \frac{\partial^2}{\partial r^2} + \left(\frac{2}{r} - \overline{R}_0 - \overline{R}_3 + \frac{1}{\overline{R}_2} \frac{\partial \overline{R}_2}{\partial r} \right) \frac{\partial}{\partial r} + \frac{\partial \overline{R}_3}{\partial r} - \frac{\overline{R}_3}{\overline{R}_2} \frac{\partial \overline{R}_2}{\partial r} + \overline{R}_0 \overline{R}_3 - \overline{R}_1 \overline{R}_3 - \left(\frac{\partial}{\partial r} + \frac{1}{r} \right) \left(\overline{R}_0 + \overline{R}_3 - \frac{1}{\overline{R}_2} \frac{\partial \overline{R}_2}{\partial r} \right), \tag{41}$$

and the functions R_i appear in the Appendix.

The boundary conditions for $p_0^\dagger$ are similar to those for $\hat{p}_0$ since (40) reduces to a similar form of Bessel's equation to give

$$p_0^\dagger \sim I_m(\overline{A}_1 r) \quad \text{as} \quad r \to 0, \tag{42}$$

$$p_0^\dagger \sim K_m(\overline{A}_2 r) \quad \text{as} \quad r \to \infty. \tag{43}$$

The solvability condition to determine $N(X)$ is obtained from the relation

$$\langle p_0^\dagger, \mathscr{L} \hat{p}_1 \rangle = \langle \mathscr{L}^\dagger p_0^\dagger, \hat{p}_1 \rangle, \tag{44}$$

which reduces to

$$\langle p_0^\dagger, h_1 \rangle = 0. \tag{45}$$

The function h_1 contains terms involving disturbances and axial derivatives of disturbances, and can therefore be written in the form

$$h_1(X, r) = \frac{\mathrm{d}N}{\mathrm{d}X} h_{11}(X, r) - N(X) h_{12}(X, r), \tag{46}$$

which means that (45) becomes

$$\frac{\mathrm{d}N}{\mathrm{d}X}\int_0^\infty \overline{p_0^\dagger}\, h_{11}(X,r) r\,\mathrm{d}r - N(X)\int_0^\infty \overline{p_0^\dagger}\, h_{12}(X,r) r\,\mathrm{d}r = 0, \tag{47}$$

or

$$F(X)\frac{\mathrm{d}N}{\mathrm{d}X} = G(X)N(X). \tag{48}$$

Thus

$$N(X) = N_0 \exp\left(\int^X \frac{G(\xi)}{F(\xi)}\,\mathrm{d}\xi\right), \tag{49}$$

where N_0 is an arbitrary normalization constant.

The general solution (49) clearly becomes singular if $F(X) = 0$ at some values of X. In order to remove the singularity a second scaling in X must be carried out, which will be described in § 6.

The unsteady pressure field can be characterized by the axial wavenumber and the cross-sectionally averaged envelope amplitude which is defined as

$$A(X) = \left[\int_0^\infty |\hat{p}_0(X,r)|^2 r\,\mathrm{d}r\right]^{1/2}. \tag{50}$$

The combined variation in the eigenfunction, $p_0(X,r)$, the amplitude, $N(X)$ and the axial wavenumber can be expressed in terms of the function

$$B(X) = A(X)\exp\left(-\frac{1}{\varepsilon}\int^X k_i(\xi)\,\mathrm{d}\xi\right), \tag{51}$$

which provides a measure of the overall growth and physical variation in the unsteady pressure with X.

5. Numerical results

In this section numerical results for instability waves of a particular jet flow are presented. The first stage is to solve the governing mean flow equations (11)–(17) numerically. The swirling jet profile at the nozzle exit is based on that studied by Lu & Lele (1999) where the initial axial and azimuthal velocities specified at $X = 0$ are

$$U_0 = \frac{1+U_2}{2} - \frac{1-U_2}{2}\tanh 2(r-R), \tag{52}$$

$$W_0 = \frac{w_{max}}{\cosh^2 2(r-R)}, \tag{53}$$

with R the jet nozzle radius. The initial temperature profile is approximated by the Crocco–Busemann relation (Young 1989) and the initial pressure is obtained by integrating the radial momentum equation (13), using (17) to eliminate the density.

The governing equations are solved numerically following the method employed by Lu & Lele (1999) which maps the equations from the semi-infinite domain $r \in (0,\infty)$ to a finite domain $\eta \in (0,1)$. The equations are then discretized using the Crank–Nicolson method. For further details on the computation the reader is referred to Lu & Lele (1999).

The evolution of the mean flow components is shown in figure 1, where $U_2 = 0.5$, $T_2 = 1$, $R = 10$, $w_{max} = 1$ and $M = 1.6$. The ratio of specific heats and Prandtl number are taken throughout to be $\gamma = 1.4202$ and $\sigma = 0.7$ respectively. The swirl profile

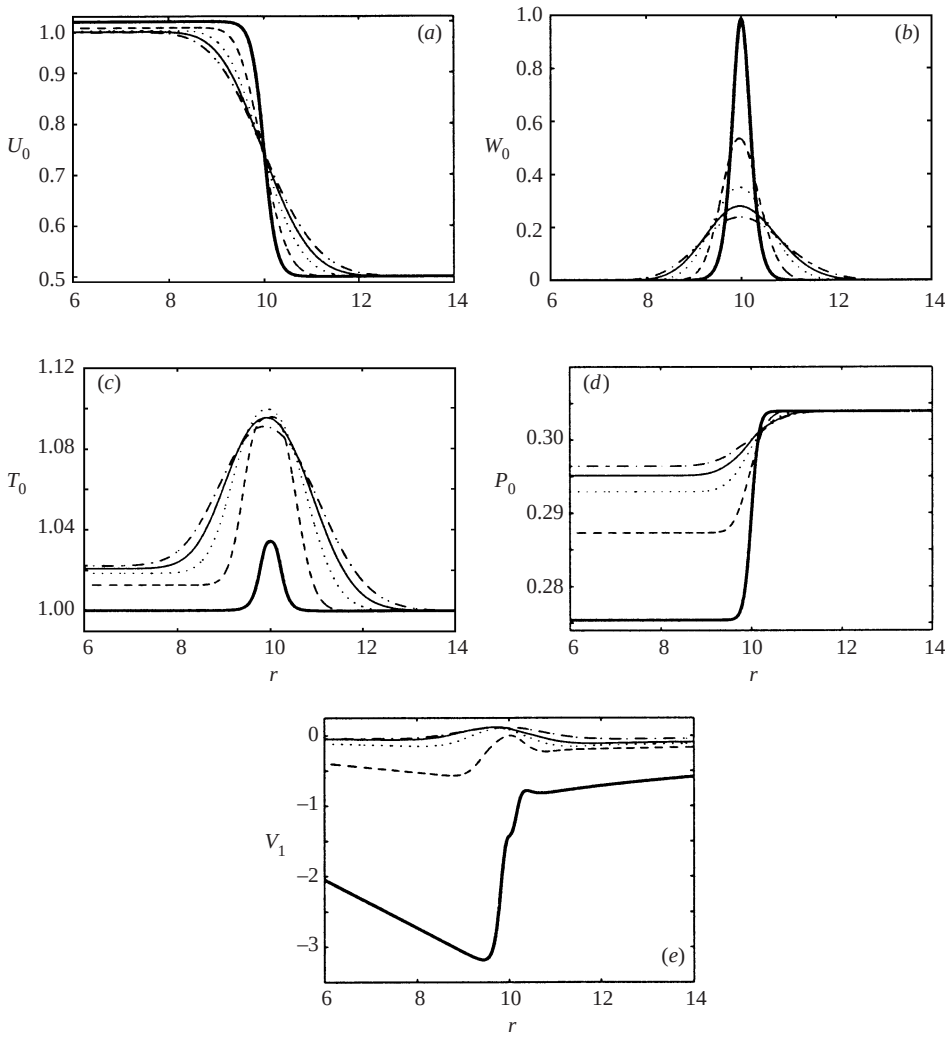

FIGURE 1. Mean flow solution: (*a*) U_0, (*b*) W_0, (*c*) T_0, (*d*) P_0, (*e*) V_1. Bold line denotes initial X-station, dashed line: $X = 0.1$, dotted line: $X = 0.3$, solid line: $X = 0.5$, dash-dot line: $X = 0.7$.

spreads out and decreases in amplitude with downstream distance, and entrainment, as expressed by the (negative) radial velocity εV_1, also decreases downstream.

In determining the disturbance field we return to the semi-infinite domain and subsequently truncate this at an outer radius of $r_{out} = 25$. The leading-order disturbance field is determined by the homogeneous eigenvalue problem in (33) which is solved numerically using a Runge–Kutta integration scheme. Throughout the computation the domain $r \in [0, r_{out}]$ is discretized using 10 000 equally spaced points and an X-step of 0.002 used. This was found to be sufficient to ensure convergence of all eigenfunctions and the final result for the amplitude. Initial guesses for the shooting method were obtained based on the grid search method of Tam & Hu (1989).

For the spatial stability problem real values of ω and integer values of m are specified and a complex value of k determined. Using the boundary conditions in (36) and (37), and an initial estimate for k, the $n = 0$ equation in (33) is integrated

from r near zero and for r large. The eigenvalue k is obtained by using Newton iteration to match smoothly each of the solutions at some intermediate point. Once k has been calculated the associated eigenfunctions determine the functions $F(X)$ and $G(X)$ in (49). For symmetry reasons, and to compare results with Lu & Lele (1999), m is restricted to positive integer values and ω is allowed to be positive or negative. Therefore when $\omega > 0$ modes are co-rotating with the swirl and when $\omega < 0$ the modes are counter-rotating.

The axisymmetric swirling jet supports two types of unstable mode. One is the Kelvin–Helmholtz shear instability arising due to the axial velocity gradient, and is present in a non-swirling jet. The second is a centrifugal mode which is present only in swirling jet flows and becomes centrifugally unstable since rW_0 decreases with r.

Tam & Burton (1984*a*, *b*) describe how the position of the trajectory of the eigenvalue in relation to the branch points of the argument A_2 in (35) must be considered for the calculation of damped modes and how this has implications for sound radiation into the far field. The branch points of A_2 lie at

$$\frac{\omega M}{1 + MU_2}, \quad \frac{-\omega M}{1 - MU_2}, \tag{54}$$

and the branch cuts run from the branch points towards the origin and along the positive/negative imaginary axis respectively. Waves in the fourth quadrant of the k-plane to the right of the branch point propagate with subsonic phase velocities relative to the ambient sound speed. Those to the left of the branch point propagate with supersonic phase velocities and it is these which radiate sound into the far field. Typical trajectories are shown in figure 2 for different degrees of mean swirl. For sufficiently high swirl the Kelvin–Helmholtz waves propagate with supersonic phase velocities, but for the example shown, the trajectory crosses into the subsonic phase velocity regime when $w_{max} \leqslant 0.2$. The centrifugal mode, for the parameters chosen, becomes stable when $w_{max} \leqslant 0.6$ and the trajectories lie in the third quadrant away from the branch cut. The growth rate of both modes decreases as the amount of swirl decreases.

Generally the trajectories of the unstable modes lie in the region between the branch points and run into the branch cut on the real axis as the mode becomes neutrally stable, and the computation is stopped here. In order to continue into the damped regime the method of matched asymptotic expansions must be applied, as discussed by Tam & Morris (1980) and Tam & Burton (1984*a*, *b*). In practice the problem of reaching the branch cut and finding the stable modes can be overcome by analytically continuing the trajectory onto the second Riemann sheet of A_2. Tam & Morris (1984) and Tam & Burton (1984*a*, *b*) also discuss a second modification to the numerical procedure which must be applied to determine the damped modes. A critical point, r_c, is the radius at which $E(r_c) = 0$ and the integration contour must always pass below this point. In the case of unstable modes the critical point lies in the upper half of the complex r-plane and the integration contour can be taken along the real axis. As the mode becomes more stable r_c moves down and hits the real axis when the mode is neutrally stable. When the mode is damped the critical point is located in the lower half of the complex r-plane and the integration contour must be deformed off the real axis. This is in general non-trivial owing to the fact that the mean flow is obtained numerically and in order to determine the location of the critical point it would be necessary to analytically continue the mean flow solutions into the complex r-plane. This is not attempted here since the primary interest is in the evolution of the modes in the unstable regime. Continuation into the stable

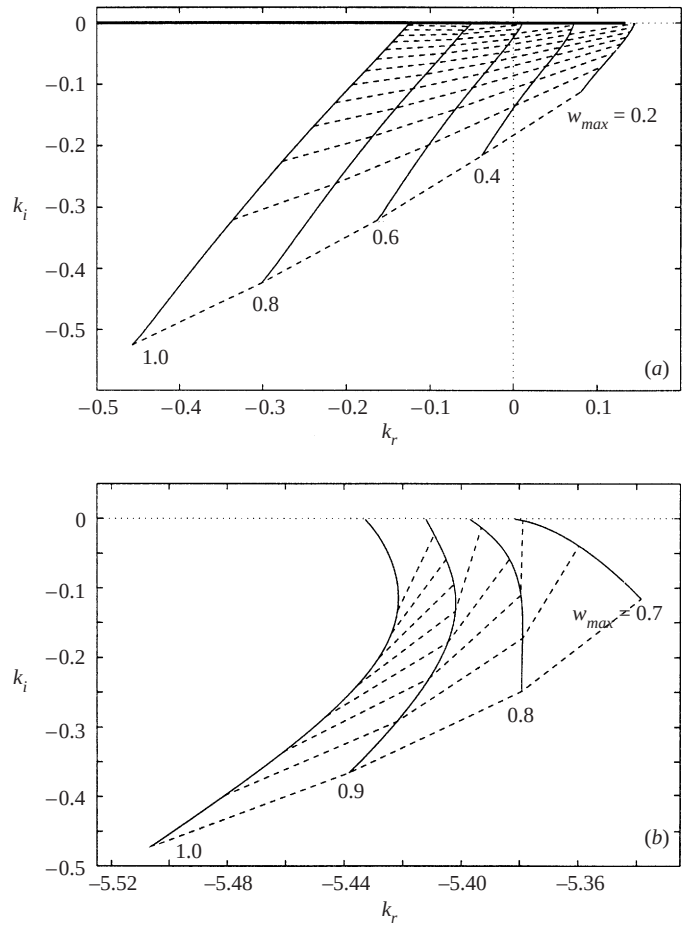

FIGURE 2. Variation in trajectory of eigenvalues in the complex k-plane with degree of mean swirl. Solid lines show the trajectory for a given mean swirl, the dashed lines indicate the X-location and the bold line shows the location of the branch cut. (a) Shear mode $m = 16$, $\omega = 0.15$, with the X-location shown in steps of 0.05. The branch points lie at $k_r = 0.133$ and $k_r = -1.2$. (b) Centrifugal mode $m = 10$, $\omega = -2.82$, with the X-location shown in steps of 0.0075. The branch points are located at $k_r = 15.6$ and $k_r = -1.733$. All curves start from $X = 0$, and in each case increasing X is in the direction in which k_i becomes less negative. The parameters used are $M = 1.6$, $U_2 = 0.5$, $T_2 = 1$, $R = 10$, $\sigma = 0.7$.

region would be required, however, in order to determine the sound generated by the instability waves as in Tam & Burton (1984*a*, *b*).

For a prescribed mean flow the stability of the system depends on four parameters, ω, m, X and w_{max}, and so an exhaustive study across the whole parameter range is beyond the scope of the paper. Attention is therefore restricted mainly to the evolution of waves which are most instable at the nozzle exit. All results presented are for the mean flow parameters $M = 1.6$, $U_2 = 0.5$, $T_2 = 1$, $\gamma = 1.4202$, $\sigma = 0.7$ and $R = 10$.

The first set of results concerns the Kelvin–Helmholtz shear mode where the influence of w_{max} is also addressed. At the initial X-station the mode which is most unstable is found to be $m = 28$, $\omega = 0.6425$, and for each m co-rotating modes are more unstable than counter-rotating ones. The downstream evolution of this mode, and other azimuthal modes at frequencies which are most amplified at the nozzle exit,

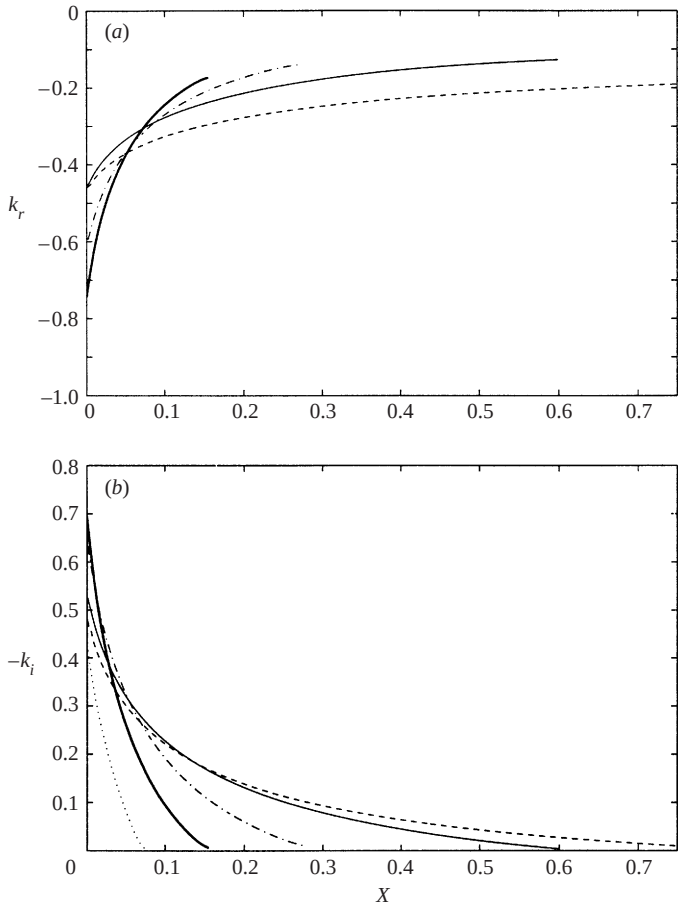

FIGURE 3. Eigenvalues for shear instability as a function of X at the frequency which gives the most amplified mode at $X = 0$. (a) k_r, (b) $-k_i$. Dotted line: $m = 10$, $\omega = 2.12$ ($k_r > 0$, not shown); solid line: $m = 16$, $\omega = 0.15$; dash-dot line: $m = 22$, $\omega = 0.37$; bold line: $m = 28$, $\omega = 0.6425$; dashed line: $m = 14$, $\omega = 0.01$.

are given in figure 3. Non-parallel effects curtail the unlimited growth predicted by the parallel flow approximation and the waves become more stable as they propagate downstream. Although the Kelvin–Helmholtz wave with $m = 28$ is the most unstable at the nozzle exit, other azimuthal wavenumbers have a slower rate of decay, and the mode found to persist the furthest downstream is for $m = 14$. Note that for all values of m the case of vanishing $|k|$ is not encountered.

Figure 4(a) shows the cross-sectionally averaged envelope amplitudes for the modes in figure 3. The function $B(X)$ is plotted in figure 4(b) where a value of $\varepsilon = 0.005$ has been assumed. These results are dominated by the exponential factor in (51) involving the growth rate and all curves reach a maximum at some value of X. By differentiating (51) with respect to X it can be deduced that the maximum in B arises for a weakly amplified mode. The results show that even though the envelope amplitude A decreases quite rapidly, it is not sufficient to significantly attenuate the growth of these unstable modes.

The effect of changing the degree of initial swirl on the $m = 16$ mode is shown in figure 5, where as w_{max} is decreased both the magnitude of the unstable eigenvalue

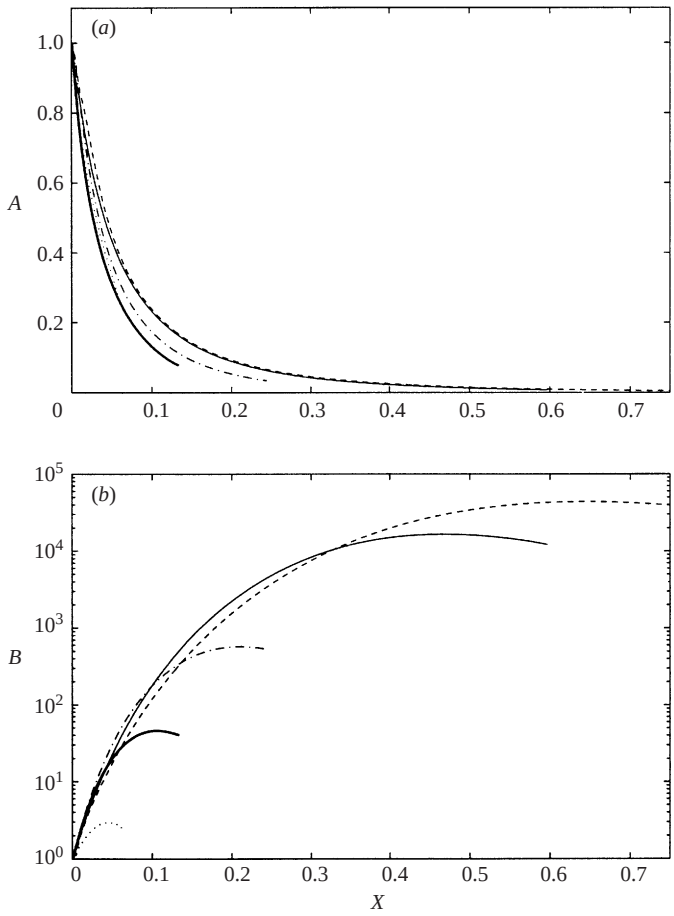

FIGURE 4. Evolution of the shear instability. (*a*) Cross-sectionally averaged amplitude normalized to unity at the nozzle exit, (*b*) $B(X)$ plotted on log scale. Dotted line: $m = 10$, $\omega = 2.12$; solid line: $m = 16$, $\omega = 0.15$; dash-dot line: $m = 22$, $\omega = 0.37$; bold line: $m = 28$, $\omega = 0.6425$, dashed line: $m = 14$, $\omega = 0.01$.

and the overall growth envelopes decrease. An interesting observation is the shape of the eigenvalue profiles at the nozzle exit (shown as an inset in figure 5*a*). These have a bi-modal distribution with the most amplified frequency switching from one maximum to the other between $w_{max} = 0.8$ and $w_{max} = 0.6$. The effect of this switching in frequency is reflected in the more rapid decay in $|k_i|$ for values of $w_{max} \leqslant 0.6$.

It should be noted that as w_{max} decreases, the azimuthal mode number which persists furthest downstream also decreases, and the general trend in figure 5(*b*) is not observed in all cases. The most amplified mode for this non-swirling jet occurs when $m = 0$, and in this case even though $|k_i|$ is greater for the swirling jet, the overall growth envelope is larger for the non-swirling jet. In summary though, adding swirl to the axisymmetric jet results in much larger overall growth.

For the centrifugal instability only counter-rotating modes are unstable at the initial X-station, and figure 6 shows the axial evolution of the eigenvalues at the most amplified frequency when $m = 10$ and $m = 16$. In contrast to the Kelvin–Helmholtz waves the mode which is most unstable at the nozzle exit remains the most unstable as it propagates downstream, and is in agreement with the results in Lu & Lele (1999) where the amplification rate was found to increase with m.

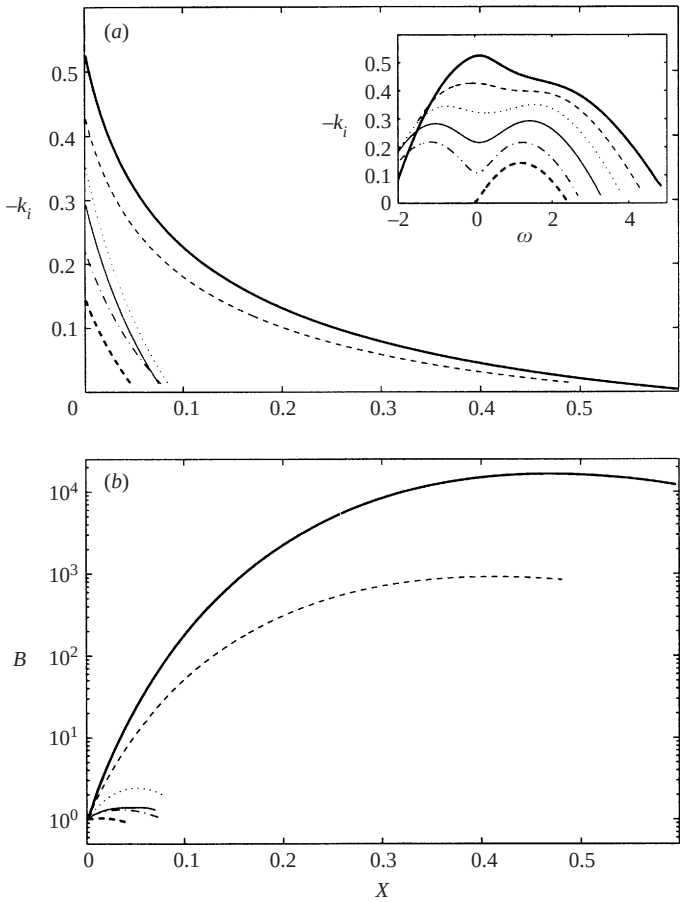

FIGURE 5. Effect of w_{max} on the shear instability when $m = 16$. (a) $-k_i$. Inset shows distribution of eigenvalues with frequency at the nozzle exit, (b) $B(X)$ plotted on log scale. Bold solid line: $w_{max} = 1$, $\omega = 0.15$; dashed line: $w_{max} = 0.8$, $\omega = -0.02$; dotted line: $w_{max} = 0.6$, $\omega = 1.533$; $w_{max} = 0.4$, $\omega = 1.41$; dash-dot line: $w_{max} = 0.2$, $\omega = 1.235$; bold dashed line: $w_{max} = 0$, $\omega = 1.198$.

Figure 7(a) shows a much more rapid attenuation of A for the centrifugal mode compared to the Kelvin–Helmholtz mode. This is reflected subsequently in the values of $B(X)$. A significant result here is that the decay in amplitude of the centrifugal mode results in very little overall growth, despite the amplification rate being comparable to that of the shear mode. Another feature in figure 7(b) is that the overall growth of the $m = 10$ mode is greater than that for $m = 16$ despite the latter having more unstable eigenvalues for all X. This is due to the faster decay in the amplitude A for the higher value of m. In Lu & Lele (1999) it was suggested that viscous effects would stabilize these modes for high values of m; here the inclusion of non-parallel (and viscous) effects is found to have a stabilizing influence on the centrifugal mode, and appears to give some support to this suggestion. We can conclude that the inclusion of non-parallel effects significantly attenuates the instability growth for centrifugal modes, and therefore presumably limits the contribution that these modes might make to mixing.

The most amplified frequency for the centrifugal mode is particularly sensitive to axial location (unlike the shear mode where the variation is less pronounced) and

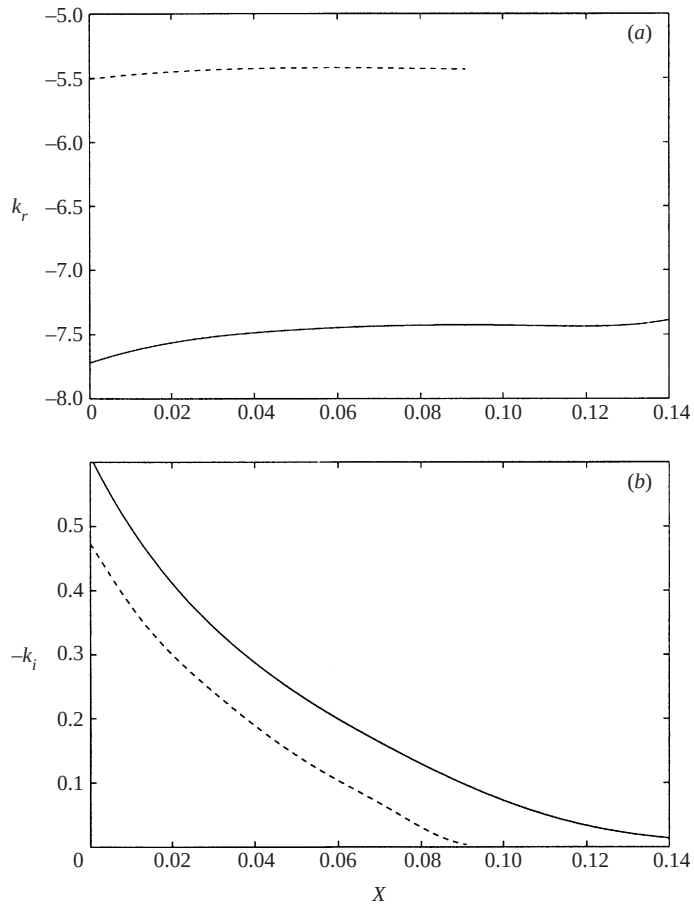

FIGURE 6. Eigenvalues for centrifugal instability as a function of X at the frequency which gives the most amplified mode at $X = 0$. (*a*) k_r, (*b*) $-k_i$. Dashed line: $m = 10$; $\omega = -2.82$, solid line: $m = 16$; $\omega = -3.77$.

it would be interesting to know whether the trend set in figure 7 continues across a range of frequencies. In order to ascertain this results have been calculated for a number of frequencies which are unstable at the initial X-location. The evolution and overall growth downstream for $m = 10$ and $m = 16$ are compared in figure 8. This shows how the eigenvalues for the $m = 16$ mode propagate further downstream, but the overall growth continues to be curtailed by the amplitude function leaving the $m = 10$ mode more amplified. In both cases the greatest overall growth occurs for frequencies which persist the longest, but the maximum envelope growth remains significantly lower than that of the shear mode.

6. Turning-point analysis

A series of neutral propagating modes is found to exist in the eigenvalue spectrum. These propagate with subsonic phase velocity and lie on the real k-axis away from the branch cuts discussed in the previous section, and thus pose no problem in computation. Since these modes have a purely real wavenumber as they propagate it is important to determine their envelope amplitude variation. In doing this it was found that for the neutral modes with $k_r > 0$ there is an axial location, X_t, at

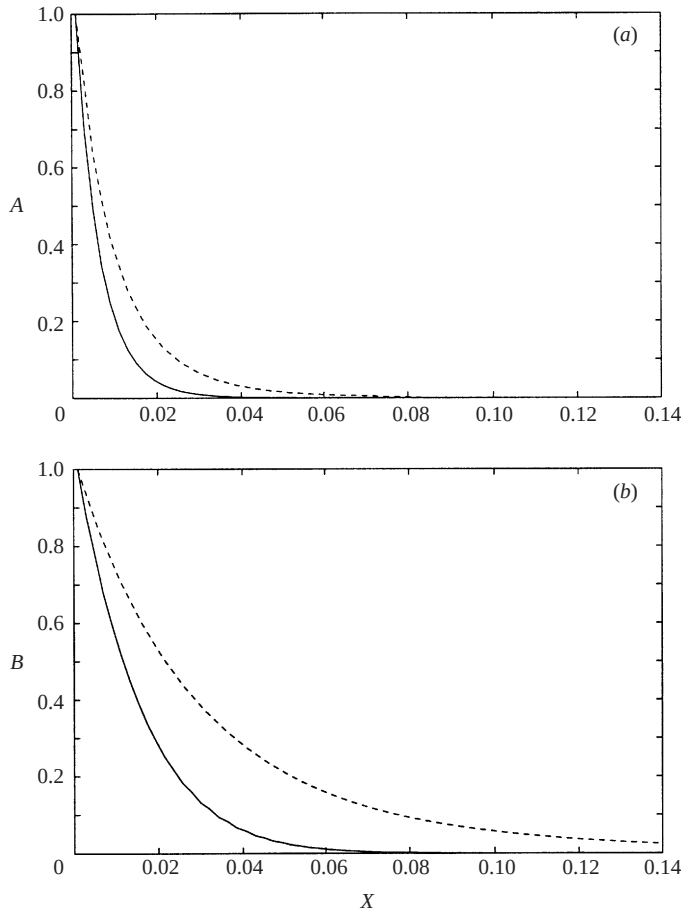

FIGURE 7. Evolution of the centrifugal instability. (*a*) Cross-sectionally averaged amplitude normalized to unity at the nozzle exit, (*b*) $B(X)$. Solid line: $m = 16$; $\omega = -3.77$, dashed line: $m = 10$; $\omega = -2.82$.

which $F(X_t) = 0$ and so the general solution (49) for the envelope amplitude breaks down. In order to remove the singularity, and obtain the slowly varying amplitude, a rescaling of the axial coordinate must be carried out and terms of $O(\varepsilon^2)$ containing second-order X-derivatives must be retained.

In general the functions F and G are complex, but for these neutral modes they are dominated by their imaginary parts. The wavenumber variation for a particular mode and the variation of $\mathrm{Im}\{F\}$, when $m = 16$ and $\omega = 0.15$, are shown in figure 9. Here it can be seen that the axial wavenumber does not undergo any particular transition when $\mathrm{Im}\{F\}$ passes through zero, unlike the case of turning points in slowly varying duct flow where a mode is propagating, or cut on, on one side of the turning point and evanescent, or cut off, on the other side. Figure 9(*b*) also shows that $\mathrm{Im}\{F(X)\}$ can be approximated by a straight line in the vicinity of the turning point. The imaginary part of $G(X)$ is positive for all values of X.

A transformation of the axial coordinate is carried out to define $\overline{X} = X - X_t$. If higher-order terms are retained in the solvability condition (48) then this becomes

$$-\mathrm{i}\varepsilon\tilde{H}(\overline{X})\tilde{N}''(\overline{X}) - \tilde{F}(\overline{X})\tilde{N}'(\overline{X}) + \tilde{G}(\overline{X})\tilde{N}(\overline{X}) = 0, \tag{55}$$

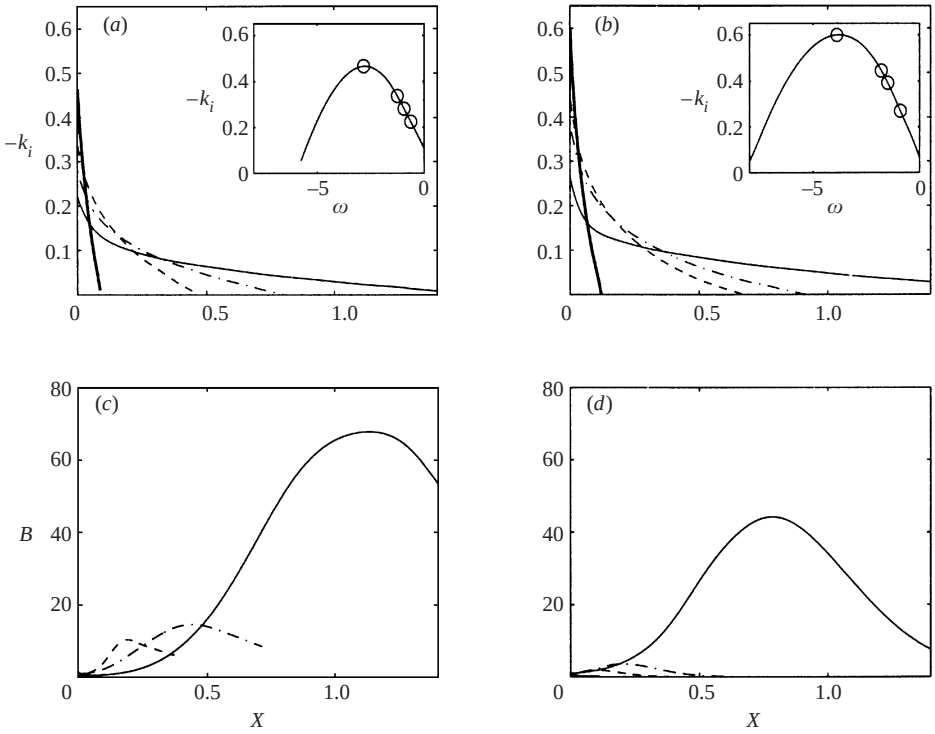

FIGURE 8. Effect of frequency on the centrifugal instability. (*a*) $m = 10$, $-k_i$, (*b*) $m = 16$, $-k_i$. In the insets the solid line shows the distribution of eigenvalues with frequency at the nozzle exit, and the circles denote the frequencies plotted in the main figures. (*c*) $B(X)$, $m = 10$, (*d*) $B(X)$, $m = 16$. Lines correspond to the frequencies which give the maximum growth rate at $X = 0$ (bold solid line), $X = 0.125$ (dashed line), $X = 0.25$ (dash-dot line) and $X = 0.5$ (solid line).

where $\tilde{F}(\overline{X}) = \mathrm{Im}\{F(X)\}$, etc. Primes denote differentiation with respect to $\overline{X}$ and for this case the solvability condition is written such that $\tilde{F}, \tilde{G}$ and $\tilde{H}$ are all real functions. If an integrating factor is introduced such that

$$\tilde{N}(\overline{X}) = M(\overline{X}) \exp\left(\frac{\mathrm{i}}{2\varepsilon}\int^{\overline{X}} \frac{\tilde{F}(\xi)}{\tilde{H}(\xi)}\,\mathrm{d}\xi\right), \tag{56}$$

then (55) can be written in the form

$$\varepsilon^2 M''(\overline{X}) = -\left[\frac{\tilde{F}^2}{4\tilde{H}^2} + \mathrm{i}\varepsilon\left\{\frac{\tilde{G}}{\tilde{H}} + \frac{1}{2}\frac{\mathrm{d}}{\mathrm{d}\overline{X}}\left(\frac{\tilde{F}}{\tilde{H}}\right)\right\}\right] M(\overline{X}). \tag{57}$$

This type of equation is discussed in Bender & Orszag (1978), and using the WKB technique the general solution away from the turning point is

$$\tilde{N}(\overline{X}) = A_{1,2}\exp\left(\int^{\overline{X}}\left[\frac{\mathrm{i}\tilde{F}(\xi)}{\varepsilon\tilde{H}(\xi)} - \frac{\tilde{G}(\xi)}{\tilde{F}(\xi)}\right]\mathrm{d}\xi\right)\left(\frac{\tilde{H}}{\tilde{F}}\right) + B_{1,2}\exp\left(\int^{\overline{X}}\frac{\tilde{G}(\xi)}{\tilde{F}(\xi)}\,\mathrm{d}\xi\right), \tag{58}$$

where subscripts 1 and 2 refer to the regions $\overline{X} < 0$ and $\overline{X} > 0$ respectively. Since $\tilde{G}/\tilde{F} > 0$ when $\overline{X} > 0$ we must have $B_2 = 0$ to eliminate the exponentially growing solution.

In the inner region close to the turning point the leading-order expansion of $\tilde{F}(\overline{X})$,

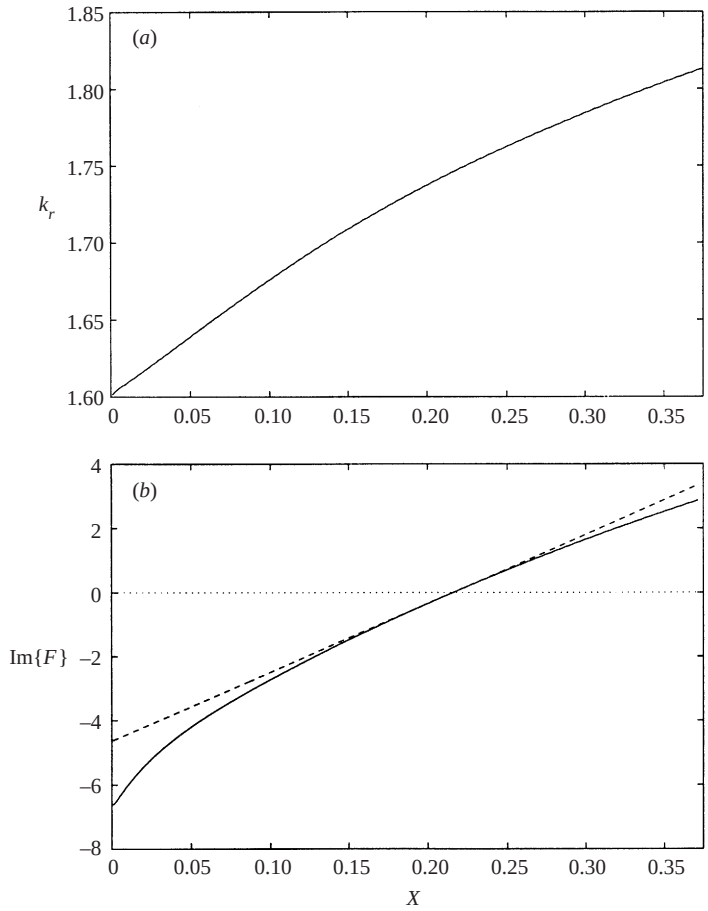

FIGURE 9. Neutral mode when $m = 16$, $\omega = 0.15$. (a) Axial wavenumber variation. (b) Solid line shows the function $F(X)$ which passes through zero at $X = X_t$. The dashed line shows the linear behaviour of $\mathrm{Im}\{F\}$ in the vicinity of X_t.

as shown in figure 9(b), can be expressed as

$$\tilde{F}(\overline{X}) = a_0\overline{X}, \quad a_0 > 0. \tag{59}$$

If the other functions are expanded about $\overline{X} = 0$, such that $\tilde{G}(0) = G_0$ and $\tilde{H}(0) = H_0$ denote the values at the turning point, and the axial coordinate rescaled according to

$$\overline{X} = \varepsilon^{1/2} a^{-1/2} \mathrm{e}^{-\mathrm{i}\pi/4} y, \tag{60}$$

where $a = a_0/|H_0| > 0$, then the inner region is governed by the equation

$$\frac{\mathrm{d}^2 M}{\mathrm{d}y^2} + \left(\nu + \frac{1}{2} - \frac{y^2}{4}\right) M = 0, \tag{61}$$

where $\nu = -1 - G_0/a_0$.

The general solution to (61) can be written in terms of parabolic cylinder functions, as

$$M(y) = c_1 D_\nu(y) + c_2 D_\nu(-y). \tag{62}$$

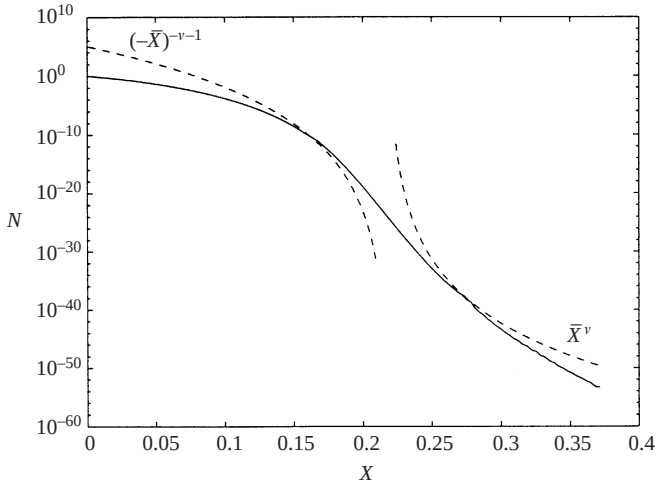

FIGURE 10. Amplitude variation for the neutral mode shown in figure 9. The solid line is the composite of the numerical outer solution and the inner solution given by the parabolic cylinder function. The numerical solution breaks down near the turning point (located at $X = 0.216$). The dashed lines represent the outer behaviour of the parabolic cylinder function and also the behaviour of the numerical solution in the vicinity of the turning point.

The constants $A_{1,2}$, B_1, c_1 and c_2 can be determined by asymptotic matching in the appropriate limits. The outer solution (58) as $\overline{X} \to 0^{\pm}$ is matched to the inner solution as $y \to \pm\infty$. Using the asymptotic expansions of the parabolic cylinder functions (see Bender & Orszag 1978) we find that

$$c_2 = 0, \tag{63}$$

$$A_{1,2} = -c_1 a \mathrm{e}^{\mathrm{i}\pi\nu/2} \left(\frac{a}{\varepsilon}\right)^{\nu/2}, \tag{64}$$

$$B_1 = \frac{-c_1 (2\pi)^{1/2} \mathrm{e}^{-\mathrm{i}\pi(5\nu+1)/4}}{\Gamma(-\nu)} \left(\frac{a}{\varepsilon}\right)^{(-\nu-1)/2}. \tag{65}$$

The value of c_1 is determined from some normalization condition.

Figure 10 returns to the standard axial variable X and shows the amplitude (normalized to unity at the nozzle exit) for one of these neutral modes. The amplitude decays very rapidly due to the fact that the values of $G(X)$ are generally large and positive. The decay in amplitude is much faster as it passes through the turning-point region. In effect, the neutral modes are strongly attenuated and do not propagate far downstream. It is found that viscous effects contribute most to this rapid decay in amplitude. If all viscous terms are omitted from the unsteady disturbance equations (specifically all the terms involving T_0^n and $T_0^{n-1}\partial T_0/\partial r$ are omitted from $f_2 - f_5$ in the Appendix), then G_0 is much smaller (ν less negative), which results in a much slower decay in the amplitude of the neutral mode through the turning point. The effect of including only terms due to slow axial variation is shown in figure 11. The neutral mode still decays through the inner region, but now that the unsteady viscous and thermal terms have been removed this can only be attributed to the axial variation in the steady flow. Whether or not the unsteady terms are included, however, we can see from figures 10 and 11 that a region of relatively short-scale variation is generated around the turning point. In the absence of mean swirl these neutral modes are still found to exist, but calculations suggest that the turning points are removed.

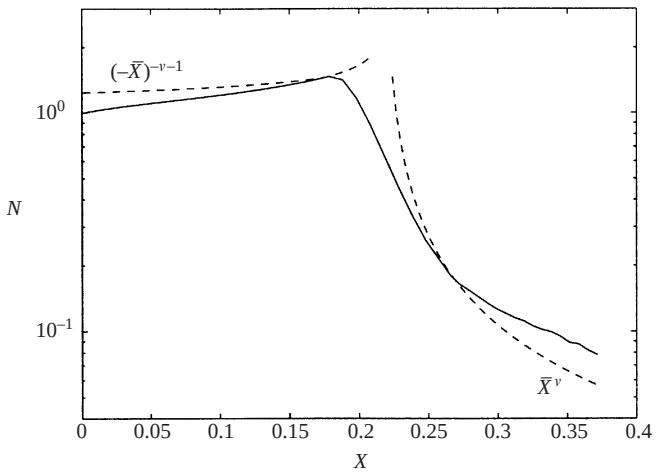

FIGURE 11. Amplitude variation for the neutral mode shown in figure 9 with viscous terms omitted from the disturbance analysis.

Tam & Burton (1984*b*), who did not include any unsteady viscous terms in their unsteady analysis, concentrated on sound radiation into the far-field from unstable modes which have much larger amplitudes than the neutral modes discussed in this paper. For the neutral modes of the swirling jet, however, the faster decay through the turning-point region may have an effect on the radiated sound field. In the absence of viscous effects the amplitude variation is similar to a Heaviside function, $H(x)$, centred on the turning point, at least on the scale of the slow X variation. Tam & Burton (1984*b*) derive a formula in which the directivity of the far-field noise is proportional to the magnitude of the Fourier transform of the modal amplitude. From Lighthill (1958) the Fourier transform of the Heaviside function is

$$\frac{1}{2\pi}\int_{-\infty}^{\infty} H(x)\,\mathrm{e}^{-\mathrm{i}\lambda x}\,\mathrm{d}x = \tfrac{1}{2}\delta(\lambda) - \frac{\mathrm{i}}{2\pi\lambda},$$

which indicates that a larger contribution to the noise from our neutral mode occurs when $\lambda \approx 0$. Comparison with Tam & Burton (1984*b*) identifies this with the sideline direction, and suggests that increased sound radiation normal to the jet axis may be observed as a result of the turning-point behaviour observed here.

7. Conclusions

There is some interest in the addition of swirl to jet flows as a means of mixing enhancement. The majority of theoretical work to date has focused on either a simplified analytical flow profile, or the parallel flow approximation with a fixed profile assumed at every axial location. Here the important effect of the divergence of the jet mean flow is included through numerical solution of the boundary-layer equations. The slow divergence of the jet and the subsequent reduction and spreading of the swirl component has a large effect on the instability growth rate. Numerical results show that the two modes of instability (shear and centrifugal) are most unstable at the nozzle exit and become less unstable as they propagate downstream. At some axial location the modes become neutrally stable and then become damped further downstream.

The growth rates of the two modes at the nozzle exit are comparable, but the amplitude of the centrifugal mode is found to be more strongly attenuated than

the shear mode. This decay in amplitude has a large counteractive effect on the axial growth of the centrifugal instability, with the overall growth of the disturbance restricted to quite modest values. In some cases the effect of the mean flow divergence on the disturbance amplitude results in a suppression of the overall growth. For the shear mode, however, the growth rate due to the axial wavenumber largely outweighs the reduction in disturbance amplitude and there is significant growth. Changes in the amount of initial swirl reveal the extent to which the growth of the shear instability is enhanced by swirl and, importantly, how this is sustained when the axial development of the mean flow is included. The existence of the centrifugal instability relies on there being a sufficient amount of initial swirl. For both instability modes it is not generally the mode which is most amplified at the start that persists the furthest downstream, and the mode with the slowest rate of decay is found to produce the largest overall amplitude. Results suggest that it is likely to be the shear mode that contributes most to the enhanced mixing that has been observed in practice.

The general solution for the disturbance amplitude breaks down at so-called turning points. This does not occur for the unstable modes discussed above, but does for a series of neutral propagating modes. Since these modes are neutral, the slow axial variation of the amplitude must be considered in order to determine to what extent the mode can actually propagate. A rescaling in an inner region around the turning point shows that the amplitude of the mode here is described in terms of parabolic cylinder functions. Numerical results show that the amplitude of these modes decays extremely rapidly, and as a result the disturbances do not propagate far downstream, despite being nominally neutral.

Extensions to this work might be to investigate other forms of the initial swirl distribution in order to determine an optimum swirl profile which maximizes the overall growth of the shear instability and which is likely to generate the most mixing enhancement. The spatial growth and decay of the disturbance amplitudes is also significant for noise radiation associated with the instability wave. In order to determine the near-field pressure distribution and the sound radiation into the far field our analysis would need to be modified by applying the method of matched asymptotic expansions (Tam & Burton 1984*a*, *b*) and calculating the amplitude of the disturbances further downstream into the stable regime. As already indicated, this is certainly possible in our analysis, although some significant numerical problems would need to be overcome.

The work described in this paper is supported by a research grant from EPSRC, reference GR/L80317.

Appendix

The terms on the right-hand side of (26)–(31) which contain non-parallel terms due to slow axial variation and viscosity are defined as

$$f_1(\hat{\boldsymbol{v}}, \hat{\rho}, \hat{p}, \hat{\tau}) = -\frac{\partial}{\partial X}(D_0\hat{u} + U_0\hat{\rho}) - \frac{1}{r}\frac{\partial}{\partial r}(rV_1\hat{\rho}), \tag{A 1}$$

$$\begin{aligned} f_2(\hat{\boldsymbol{v}}, \hat{\rho}, \hat{p}, \hat{\tau}) = {} & -D_0\left(U_0\frac{\partial\hat{u}}{\partial X} + V_1\frac{\partial\hat{u}}{\partial r} + \frac{\partial U_0}{\partial X}\hat{u}\right) - \hat{\rho}\left(U_0\frac{\partial U_0}{\partial X} + V_1\frac{\partial U_0}{\partial r}\right) - \frac{\partial\hat{\rho}}{\partial X} \\ & + T_0^n\left[\frac{1}{r}\frac{\partial}{\partial r}\left(\frac{\partial\hat{u}}{\partial r}r\right) - \frac{m^2}{r^2}\hat{u} - k^2\hat{u} + \frac{\mathrm{i}k}{3r}\frac{\partial}{\partial r}(r\hat{v}) - \frac{mk}{3r}\hat{w} - \frac{k^2}{3}\hat{u}\right] \\ & + nT_0^{n-1}\frac{\partial T_0}{\partial r}\left(\frac{\partial\hat{u}}{\partial r} + \mathrm{i}k\hat{v}\right), \end{aligned} \tag{A 2}$$

$$f_3(\hat{\boldsymbol{v}},\hat{\rho},\hat{p},\hat{\tau}) = -D_0\left(U_0\frac{\partial\hat{v}}{\partial X}+V_1\frac{\partial\hat{v}}{\partial r}+\frac{\partial V_1}{\partial r}\hat{v}\right)$$
$$+T_0^n\left[\frac{1}{r}\frac{\partial}{\partial r}\left(r\frac{\partial\hat{v}}{\partial r}\right)-\frac{m^2}{r^2}\hat{v}-k^2\hat{v}-\frac{\hat{v}}{r^2}-\frac{2\mathrm{i}m}{r^2}\hat{w}\right.$$
$$\left.+\frac{1}{3}\frac{\partial}{\partial r}\left(\frac{1}{r}\frac{\partial}{\partial r}(r\hat{v})+\frac{\mathrm{i}m}{r}\hat{w}+\mathrm{i}k\hat{u}\right)\right]$$
$$+nT_0^{n-1}\frac{\partial T_0}{\partial r}\left[2\frac{\partial\hat{v}}{\partial r}-\frac{2}{3}\left(\frac{1}{r}\frac{\partial}{\partial r}(r\hat{v})+\frac{\mathrm{i}m}{r}\hat{w}+\mathrm{i}k\hat{u}\right)\right], \tag{A 3}$$

$$f_4(\hat{\boldsymbol{v}},\hat{\rho},\hat{p},\hat{\tau}) = -D_0\left(U_0\frac{\partial\hat{w}}{\partial X}+V_1\frac{\partial\hat{w}}{\partial r}+\frac{\partial W_0}{\partial X}\hat{u}+\frac{V_1\hat{w}}{r}\right)$$
$$-\hat{\rho}\left(U_0\frac{\partial W_0}{\partial X}+V_1\frac{\partial W_0}{\partial r}+\frac{W_0V_1}{r}\right)$$
$$+T_0^n\left[\frac{1}{r}\frac{\partial}{\partial r}\left(r\frac{\partial\hat{w}}{\partial r}\right)-\frac{m^2}{r^2}\hat{w}-k^2\hat{w}-\frac{\hat{w}}{r^2}+\frac{2\mathrm{i}m}{r^2}\hat{v}\right.$$
$$\left.+\frac{\mathrm{i}m}{3r^2}\left(\frac{1}{r}\frac{\partial}{\partial r}(r\hat{v})+\frac{\mathrm{i}m}{r}\hat{w}+\mathrm{i}k\hat{u}\right)\right]+nT_0^{n-1}\frac{\partial T_0}{\partial r}\left[\frac{\partial\hat{w}}{\partial r}-\frac{\hat{w}}{r}+\frac{\mathrm{i}m\hat{v}}{r}\right], \tag{A 4}$$

$$f_5(\hat{\boldsymbol{v}},\hat{\rho},\hat{p},\hat{\tau}) = (\gamma-1)M^2\left(U_0\frac{\partial\hat{p}}{\partial X}+V_1\frac{\partial\hat{p}}{\partial r}+\frac{\partial P_0}{\partial X}\hat{u}\right)-D_0V_1\frac{\partial\hat{\tau}}{\partial r}$$
$$-\hat{\rho}\left(U_0\frac{\partial T_0}{\partial X}+V_1\frac{\partial T_0}{\partial r}\right)-D_0\frac{\partial T_0}{\partial X}\hat{u}$$
$$+(\gamma-1)M^2T_0^n\left[\left(\frac{\partial W_0}{\partial r}-\frac{W_0}{r}\right)\left(\frac{\partial\hat{w}}{\partial r}-\frac{\hat{w}}{r}+\frac{\mathrm{i}m\hat{v}}{r}\right)+\frac{\partial U_0}{\partial r}\left(\frac{\partial\hat{u}}{\partial r}+\mathrm{i}k\hat{v}\right)\right]$$
$$+\frac{1}{\sigma}\left[\left(-k^2-\frac{m^2}{r^2}\right)T_0^n\hat{\tau}+\frac{1}{r}\frac{\partial}{\partial r}\left(rT_0^n\frac{\partial\hat{\tau}}{\partial r}\right)\right]. \tag{A 5}$$

The linear operator in (33) appears in Lu & Lele (1999) and is defined as

$$\mathscr{L}\equiv\frac{\partial^2}{\partial r^2}+\left(R_0+R_3-\frac{1}{R_2}\frac{\partial R_2}{\partial r}\right)\frac{\partial}{\partial r}+\left(\frac{\partial R_3}{\partial r}-\frac{R_3}{R_2}\frac{\partial R_2}{\partial r}+R_0R_3-R_1R_2\right), \tag{A 6}$$

where

$$R_0=\frac{1}{r}+\frac{1}{\gamma P_0}\frac{\partial P_0}{\partial r}-\frac{\mathrm{i}k}{E}\frac{\partial U_0}{\partial r}-\frac{\mathrm{i}mW_0}{Er^2}-\frac{\mathrm{i}m}{Er}\frac{\partial W_0}{\partial r}, \tag{A 7}$$

$$R_1=\frac{E}{\gamma P_0}+\frac{k^2}{ED_0}+\frac{m^2}{Er^2D_0}, \tag{A 8}$$

$$R_2=D_0E+\frac{2D_0W_0^2}{Er^2}+\frac{2D_0W_0}{Er}\frac{\partial W_0}{\partial r}+\frac{W_0^2}{Er}\frac{\partial D_0}{\partial r}-\frac{W_0^2D_0}{Er}\frac{1}{\gamma P_0}\frac{\partial P_0}{\partial r}, \tag{A 9}$$

$$R_3=\frac{2\mathrm{i}mW_0}{Er^2}-\frac{W_0^2D_0}{r\gamma P_0}, \tag{A 10}$$

The inhomogeneous terms, h_n, in (33) are given by

$$h_n=\frac{\partial\phi_n}{\partial r}-\frac{\phi_n}{R_2}\frac{\partial R_2}{\partial r}+R_0\phi_n-R_2\psi_n, \tag{A 11}$$

where

$$\phi_n = f_3(\zeta_{n-1}) + \frac{2W_0 f_4(\zeta_{n-1})}{Er} - \frac{W_0 D_0 f_5(\zeta_{n-1})}{Er\gamma P_0}, \tag{A 12}$$

$$\psi_n = \frac{f_5(\zeta_{n-1})}{\gamma P_0} + \frac{f_1(\zeta_{n-1})}{D_0} - \frac{\mathrm{i}k f_2(\zeta_{n-1})}{ED_0} - \frac{\mathrm{i}m f_4(\zeta_{n-1})}{ErD_0}, \tag{A 13}$$

with $\zeta_n = [\hat{\boldsymbol{v}}_n, \hat{\rho}_n, \hat{p}_n, \hat{\tau}_n]$.

REFERENCES

Bender, C. M. & Orszag, S. A. 1978 *Advanced Mathematical Methods for Scientists and Engineers.* McGraw-Hill.

Bouthier, M. 1972 Stabilité linéaire des écoulements presque parallès. Partie I. *J. Méc.* **11**, 599–621.

Bouthier, M. 1973 Stabilité linéaire des écoulements presque parallès. Partie II. La Couche Limite de Blasius. *J. Méc.* **12**, 75–95.

Crighton, D. G. & Gaster, M. 1976 Stability of slowly diverging jet flow. *J. Fluid Mech.* **77**, 397–413.

Cutler, A. D., Levey, B. S. & Kraus, D. K. 1995 Near-field flow of supersonic swirling jets. *AIAA J.* **33**, 876–881.

Hu, G. H., Sun, D. J. & Yin, X. Y. 2001 A numerical study of dynamics of a temporally evolving swirling jet. *Phys. Fluids* **13**, 951–965.

Khorrami, M. R. 1995 Stability of a compressible axisymmetric jet. *AIAA J.* **33**, 650–658.

Lighthill, M. J. 1958 *An Introduction to Fourier Analysis and Generalised Functions.* Cambridge University Press.

Lim, D. W. & Redekopp, G. 1998 Absolute instability conditions for variable density, swirling jet flows. *Eur. J. Mech.* B/*Fluids* **17**, 165–185.

Loiseleux, T., Delbende, I. & Huerre, P. 2000 Absolute and convective instabilities of a swirling jet/wake shear layer. *Phys. Fluids* **12**, 375–380.

Lu, G. & Lele, S. K. 1994 On the density ratio effect on the growth rate of a compressible mixing layer. *Phys. Fluids* **6**, 1073–1075.

Lu, G. & Lele, S. K. 1999 Inviscid instability of compressible swirling mixing layers. *Phys. Fluids* **11**, 450–461.

Martin, J. E. & Meiburg, E. 1994 On the stability of the swirling jet shear layer. *Phys. Fluids* **6**, 424–429.

Naughton, J. W., Cattafesta III, L. N. & Settles, G. S. 1997 An experimental study of compressible turbulent mixing enhancement in swirling jets. *J. Fluid Mech.* **330**, 271–305.

Sarasúa, L. G. & Schifino, A. C. S. 2000 Viscosity influence on the stability of a swirling jet with nonrotating core. *Phys. Fluids* **12**, 1607–1610.

Stott, J. A. K. & Duck, P. W. 1994 The stability of a trailing-line vortex in compressible flow. *J. Fluid Mech.* **269**, 323–351.

Tam, C. K. W. & Burton, D. E. 1984*a* Sound generated by instability waves of supersonic flows. Part 1. Two-dimensional mixing layers. *J. Fluid Mech.* **138**, 249–271.

Tam, C. K. W. & Burton, D. E. 1984*b* Sound generated by instability waves of supersonic flows. Part 2. Axisymmetric jets. *J. Fluid Mech.* **138**, 273–295.

Tam, C. K. W. & Hu, F. Q. 1989 On the three families of instability waves of high-speed jets. *J. Fluid Mech.* **201**, 447–483.

Tam, C. K. W. & Morris, P. J. 1980 The radiation of sound by the instability waves of a compressible plane turbulent shear layer. *J. Fluid Mech.* **98**, 349–381.

White, F. M. 1991 *Viscous Fluid Flow*, 2nd edn. McGraw-Hill.

Wu, C., Farokhi, S. & Taghavi, R. 1992 Spatial instability of a swirling jet – theory and experiment. *AIAA J.* **30**, 1545–1552.

Young, A. D. 1989 *Boundary Layers.* AIAA.